Materials Advances

ROYAL SOCIETY OF CHEMISTRY

PAPER

View Article Online
View Journal

Cite this: DOI: 10.1039/d5ma00889a

A synergistic ZnS/MWCNT heterostructure as an advanced electrode for high-performance, long-cycle life lithium-ion batteries: experimental and DFT insights

Marrium Shabbir,[ab] Rizwan Akram,[b] Saqib Javed,[c] Zahid Abbas,[ad] Amina Zafar,[e] Sheeraz Mehboob,[f] Shafqat Karim,[a] Luqman Ali,[ag] Shahid Ali,[ad] Imran Shakir,[h] Amjad Nisar *[a] and Mashkoor Ahmad *[a]

Received 12th August 2025,
Accepted 2nd November 2025

DOI: 10.1039/d5ma00889a

rsc.li/materials-advances

The synergistic integration of nanomaterials in heterostructures presents significant potential for the development of high-performance energy storage devices. In this work, a zinc sulfide/multi-walled carbon nanotube (ZnS/MWCNT) heterostructure is rationally designed and systematically investigated as a promising anode material for lithium-ion batteries (LIBs). Structural and microscopic analyses confirm that the heterostructure possesses a high specific surface area and enhanced electrical conductivity, making it highly suitable for efficient lithium storage. The ZnS/MWCNT anode delivers an impressive initial discharge capacity of 1960 mA h g^{-1} at a current density of 50 mA g^{-1} (*vs.* Li/Li^+), along with a high coulombic efficiency of approximately 97.6%. Notably, it exhibits outstanding cycling stability, retaining ~94% of its capacity after 1000 cycles. Electrochemical impedance spectroscopy (EIS) and density functional theory (DFT) analyses further reveal significantly enhanced charge transfer kinetics and lithium-ion diffusion within the heterostructure. The superior electrochemical performance is attributed to the synergistic interaction between the ZnS and MWCNTs, the robust structural integrity of the heterostructure, and its large active surface area. Moreover, the designed architecture effectively mitigates volume expansion and structural degradation during repeated charge/discharge cycles. These findings highlight the great potential of ZnS/MWCNT heterostructures as advanced anode materials for next-generation LIBs with high-rate capability and long-term cycling stability.

1. Introduction

As industries and economies continue to grow, energy remains a critical factor in meeting current and future demands. The steady rise in energy consumption calls for a shift toward clean, sustainable, and renewable sources to reshape the global economy. However, effective energy storage systems are essential to regulate and stabilize energy production, making the development of advanced, large-scale rechargeable storage technologies imperative.[1–4] To date, various storage devices, including batteries, fuel cells and supercapacitors have been designed to harness energy from renewable sources. Out of these, lithium-ion batteries (LIBs) have emerged as dominant power sources for portable electronics and hybrid electric vehicles due to their high energy density[5,6] and absence of memory effect.[7,8] Despite these advantages, LIBs face significant challenges, such as large volume changes during lithium insertion and extraction, which cause electrode pulverization, rapid capacity fading, and poor cycling stability. In addition, slow diffusion kinetics and low rate capability, limited by electrode materials, hinder the performance of current LIBs. Addressing these limitations and developing next-generation battery materials with improved portability, higher energy efficiency, and enhanced stability is crucial to meet the growing demands of modern energy storage and conversion systems.[9–16]

Currently, transition metal sulfides (TMS), like ZnS, MoS_2, CuS, SnS_2, and TiS_2, have attracted significant attention as

[a] Nanomaterials Research Group, Physics Division, PINSTECH, Islamabad 44000, Pakistan. E-mail: mashkoorahmad2003@yahoo.com, chempk@gmail.com.com
[b] Department of Applied Physics, Air University, Islamabad, Pakistan
[c] Theoretical Physics Division, PINSTECH, Islamabad 44000, Pakistan
[d] Department of Chemistry Govt. College University, Faisalabad, Pakistan
[e] Central Analytical Facility Division, PINSTECH, Islamabad 44000, Pakistan
[f] Chemistry Division, PINSTECH, Islamabad 44000, Pakistan
[g] Department of Chemistry, University of Poonch, Rawalakot, Pakistan
[h] Department of Physics, Faculty of Science, Islamic University of Madinah, Madinah 42351, Saudi Arabia

high-performance anode materials for LIBs, owing to their high theoretical capacities, rich redox chemistry and favourable electrochemical properties. As a prominent TMS, ZnS presents compelling advantages for advanced battery technologies, boasting a high theoretical specific capacity (962.3 mA h g^{-1}), strong electrochemical properties, low cost, environmental friendliness and abundant availability.[17–19] Despite these figures of merit, ZnS electrodes face significant limitations, including significant volume changes during lithiation/delithiation causing structural degradation, poor electrical conductivity,[20–22] and rapid capacity fading upon extended cycling.[23–30] To overcome these limitations, researchers have developed diverse composite strategies. These include incorporating carbonaceous materials (graphene, CNTs), integrating metal oxides (TiO_2), combining with metal nanoparticles and developing composites with conducting polymers (PANI)[31–35] in order to boost electrochemical performance. Interestingly, stitching of dissimilar dimensional materials has been revealed as an effective strategy to enhance the energy storage applications.[36] Most notably, multiwall carbon nanotubes (MWCNTs), as typical one-dimensional (1D) nanomaterials, are widely regarded as ideal building blocks owing to their exceptional high electrical conductivity, remarkable mechanical stability and large specific surface area for constructing three-dimensional (3D) network nanostructures.[37] Consequently, MWCNTs are assumed to significantly enhanced the electrical conductivity of ZnS composites and effectively overpower the mechanical degradation of ZnS during repeated charging–discharging cycles in supercapacitor and battery applications. Regarding battery applications, for instance, Cao *et al.* fabricated a core–shell MWCNTs@ZnS electrode by atomic layer deposition for high-performance LIBs exhibiting stable discharge capacity of 520 mA h g^{-1} at 100 mA g^{-1} after 200 cycles.[38] Similarly, Fan *et al.* developed a 3D ZnS/MWCNTs nanocomposite that demonstrates outstanding electrochemical performance as a sodium-ion battery anode, including high reversible capacity of 230 mA h g^{-1} at 1 A g^{-1} after 400 cycles, cycling performance (397 mA h g^{-1} at 100 mA g^{-1} after 50 cycles) and rate capability (320 mA h g^{-1} at 4 A g^{-1} after 300 cycles).[37] Furthermore, Shi *et al.*, demonstrated a CNT/ZnS-QD composite, achieving a high capacity retention of 73.4% (771 mA h g^{-1}) after 150 cycles at 0.5C.[39] Nevertheless, these studies involved complex architectures with low initial discharge capacity and less cycling stability. Therefore, it is of great interest to investigate the role of ZnS/MWCNTs to achieve excellent outcomes regarding enhanced capacity retention and rate capability in LIB electrodes.

In this work, we synthesized ZnS/MWCNTs heterostructured *via* a simple solvothermal method, achieving a high-purity material with enhanced yield. The heterostructure integrated the high theoretical capacity of ZnS with the excellent conductivity, structural stability, and large surface area of MWCNTs, resulting in improved capacity retention, rate performance, and long-term cycling stability. Such synergistic features highlight the potential of this heterostructure as a promising electrode architecture for next-generation lithium-ion batteries.

2. Experimental

2.1. Reagents and materials

All chemicals used in this study were of analytical grade and utilized without further purification. Multiwalled carbon nanotubes (MWCNTs) with lengths of several micrometers and diameters ranging from 50 to 100 nm were sourced from Nanoshel, USA. Hydrochloric acid (HCl), ethylene glycol, cetyltrimethylammonium bromide (CTAB), zinc nitrate hexahydrate ($Zn(NO_3)_2{\cdot}6H_2O$), and thioacetamide (CH_3CSNH_2) were purchased from Sigma-Aldrich. Ethanol was obtained from AnalaR. Deionized water (DI) was used exclusively throughout the synthesis and characterization processes.

2.2. Functionalization of MWCNTs

Multiwall carbon nanotubes (MWCNTs) were activated using a chemical oxidation method. Initially, 20 mL of deionized (DI) water was taken in a beaker, followed by the dropwise addition of 3 mL of HCl. Subsequently, 30 mg of untreated MWCNTs were dispersed in the acid solution and sonicated for 20 minutes at room temperature. The resulting mixture was thoroughly washed with DI water and ethanol until the pH reached near-neutral. Finally, the functionalized MWCNTs were dried in an oven at 60 °C overnight and collected for further use.

2.3. Synthesis of the ZnS/MWCNTs heterostructure

The heterostructured ZnS/MWCNTs composite was synthesized using a solvothermal method. Initially, the synthesis parameters, such as the precursor concentrations, annealing temperature, and time were carefully optimized through preliminary trials. After that, the synthesis of the final composite was carried out. Briefly, 30 mg of functionalized MWCNTs were uniformly dispersed in 10 mL of ethylene glycol under continuous magnetic stirring. Subsequently, 0.69 g of CTAB, 0.55 g of zinc nitrate hexahydrate ($Zn(NO_3)_2{\cdot}6H_2O$), and 0.15 g of thioacetamide (CH_3CSNH_2) were added to the mixture, followed by magnetic stirring for 3 hours to ensure a homogeneous solution. The prepared solution was then transferred to a 50 mL Teflon-lined stainless steel autoclave and heated at 160 °C for 12 hours. After naturally cooling to room temperature, the resulting product was centrifuged multiple times with deionized water and ethanol to remove impurities. The obtained blackish powder was dried at 60 °C for 6 hours and subsequently annealed under an argon atmosphere at 500 °C for 2 hours, yielding the final ZnS/MWCNTs heterostructure.[40] For comparison, pure ZnS was also synthesized using the same procedure, excluding the addition of MWCNTs.

2.4. Characterization of electrode materials

The structural properties of ZnS and ZnS/MWCNTs were analyzed using X-ray diffraction (XRD) with a Rigaku D/max-2500 diffractometer equipped with Cu Kα radiation (λ = 1.540405 Å). The morphology and microstructure of the samples were investigated by scanning electron microscopy (SEM) using a Tescan MIRA A3 system, coupled with an energy-dispersive

X-ray (EDX) detector for elemental analysis. High-resolution transmission electron microscopy (HRTEM, JEOL JEM-2100F, 200 kV) was employed to examine the internal structure of the samples. The elemental composition and chemical states were further characterized by X-ray photoelectron spectroscopy (XPS) using an ESCALAB 250xi instrument with a monochromatic Al Kα radiation source. Raman spectra were recorded using a Horiba Xplora Plus Raman spectrometer (France). The specific surface area was measured by the Brunauer–Emmett–Teller (BET) method, while the pore size distribution was determined using the Barrett–Joyner–Halenda (BJH) approach. Finally, Fourier-transform infrared (FTIR) spectroscopy (Thermo Scientific, USA) was performed to identify the functional groups present on the sample surfaces.

2.5. Cell assembly

The working electrode was prepared by uniformly mixing the synthesized active material, conductive carbon black, and polyvinylidene fluoride (PVDF) binder in a weight ratio of 70 : 20 : 10. The mixture was ground into a fine powder using a mortar and pestle, followed by the dropwise addition of an appropriate amount of *N*-methylpyrrolidone (NMP). The resulting slurry was magnetically stirred for 24 hours to ensure homogeneity. This uniform slurry was then coated onto copper foil using a notch bar and dried in a vacuum oven at 60 °C for 24 hours to remove residual solvent. The dried electrodes were compressed, punched into 15 mm diameter discs, and further dried under vacuum at 60 °C for another 24 hours. The mass of each electrode was recorded using a precision balance. The calculated active mass loading of the ZnS and ZnS/MWCNTs electrodes were 1.07 and 1.03 mg cm^{-2}, respectively, with 300 nm thickness. To evaluate electrochemical performance, CR2025 coin-type cells were assembled in an argon-filled glove box. For half-cell assembly, lithium metal served as the counter electrode, and 1 M lithium hexafluorophosphate ($LiPF_6$) dissolved in a 4 : 2 : 4 weight ratio mixture of ethylene carbonate (EC), diethylene carbonate (DEC), and dimethyl carbonate (DMC) was used as the electrolyte. A Celgard-2400 membrane was employed as the separator.

2.6. Electrochemical measurements

The electrochemical performance of the fabricated electrodes was evaluated through galvanostatic charge–discharge cycling at various current densities, with each test conducted for 10 cycles over a voltage window of 0.01 to 3.0 V (*vs.* Li^+/Li) using an MTI-BSTA-MA battery analyzer. A current density of 1000 mA g^{-1} was defined as 1C. The kinetic behavior of the electrodes was further investigated by cyclic voltammetry (CV) using a CHI660E electrochemical workstation (Chenhua, Shanghai, China) at a scan rate of 0.5 mV s^{-1}. Electrochemical impedance spectroscopy (EIS) was performed with a 5 mV amplitude over a frequency range of 0.01 Hz to 100 kHz to analyze the charge transfer resistance and ion diffusion characteristics.

2.7. Computational details

For the DFT calculations, the plane-wave pseudopotential method was employed using the VASP simulation package.[41] The exchange–correlation interactions were treated using the generalized gradient approximation (GGA) with the Perdew–Burke–Ernzerhof (PBE) functional.[42] A kinetic energy cutoff of 400 eV was applied, with convergence criteria set to 10^{-5} eV for total energy and 0.01 eV $Å^{-1}$ for forces. To investigate interfacial energy level alignment, multiwalled carbon nanotubes (MWCNTs) were modeled using a (4,4)@(8,8)@(12,12) three-wall configuration. For ZnS, the energetically favorable (110) surface with eight atomic layers was adopted. A vacuum spacing of 15 Å was introduced along the perpendicular direction to eliminate spurious interactions between periodic images. To accurately estimate the electronic structure and energy level alignment, hybrid HSE06 functional calculations were performed.[43] It is important to note that the electronic structures of the MWCNTs and ZnS (110) surface were calculated separately for energy level alignment analysis. This approach is computationally efficient and reasonable, as the interaction between ZnS and MWCNTs is expected to be relatively weak due to the inherent curvature of the MWCNTs.

3. Results and discussion

3.1. Morphological and structural analysis

XRD was employed to analyze the crystallinity and phase structure of the as-synthesized ZnS and ZnS/MWCNTs heterostructures. It can be seen in Fig. 1(a) that all the diffraction peaks around 28.4°, 33°, 47.5°, 56.6°, and 59.14° are indexed to the (111), (200), (220), (311), and (222) crystal planes and well match with the standard pattern of the cubic (zinc blende) phase of pure ZnS according to JCPDS card no. (01-077-2100).[35] No additional diffraction peaks are detected, demonstrating the purity of the sample. The peaks of pure ZnS are sharp and intense, indicating a higher crystallinity and larger crystallite size. On the other hand, the XRD pattern of the ZnS/MWCNTs heterostructure shows overlap with the pristine ZnS structure along with additional small diffraction peaks of MWCNTs at 27.2° and 42.8°, which are attributed to the (002) (JCPDS no. 41-1487) and (101) lattice plane.[44,45] The observed characteristic carbon peaks affirm the well-executed formation of a ZnS/MWCNT heterostructure. Moreover, the ZnS/MWCNT composite shows broader and less intense peaks, suggesting a reduction in crystallite size and increased lattice strain due to the interaction of ZnS with the MWCNTs. The average crystallite size was calculated from the peak broadening using the

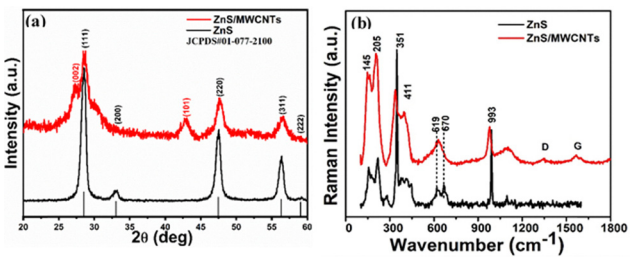

Fig. 1 (a) XRD pattern and (b) Raman spectra of the pristine ZnS and heterostructured ZnS/MWCNTs.

Scherrer equation $D = K\lambda/(\beta \cos\theta)$, where the broader peaks of the composite clearly point toward smaller nanocrystallites. The calculated average crystallite size is ~5–10 nm, consistent with the SEM and TEM results. This reduction in crystallite size enhances the surface area and can provide more active sites, which is beneficial for electrochemical applications.

Fig. 1(b) presents the Raman spectra of pristine ZnS and the ZnS/MWCNT heterostructure in the range of 100–1800 cm^{-1}. For pristine ZnS, distinct peaks are observed at 145, 205, 351, 411, 619, 670, and 993 cm^{-1}. The peaks at 145–205 cm^{-1} correspond to the transverse optical (TO) phonon mode, while the strong peak at 351 cm^{-1} is attributed to the longitudinal optical (LO) mode of cubic ZnS. The band at 411 cm^{-1} arises from the combination and splitting of low and high-frequency modes, involving both TO and longitudinal acoustic (LA) modes as well as LO and transverse acoustic (TA) modes. The peak at 619 cm^{-1} is assigned to another TO mode, and the peaks at 670 and 993 cm^{-1} correspond to additional LO modes.[46] In the ZnS/MWCNTs heterostructure, along with the characteristic ZnS signals, additional peaks at 1335 and 1573 cm^{-1} are observed, corresponding to the D and G bands of the MWCNTs, respectively.[47] The D band at 1335 cm^{-1} originates from disorder-induced phonon modes and is commonly used to assess defect density in carbon nanomaterials. The G band at 1573 cm^{-1} is associated with the stretching vibration of sp^2-hybridized C–C bonds, confirming the presence and uniform dispersion of MWCNTs within the ZnS matrix. The intensity ratio of the D to G bands (I_D/I_G) offers insight into structural defects. For the ZnS/MWCNTs heterostructure, the I_D/I_G ratio is 0.87, slightly higher than that of pristine MWCNTs (0.83), indicating the introduction of defects due to functionalization. This is attributed to the incorporation of functional groups, which induce structural distortions. This comparison highlights the degree of defect introduction and confirms the preservation of structural integrity after ZnS incorporation. The observed I_D/I_G ratio is also well matched with the previously reported work.[48–50] Additionally, a noticeable shift of the D and G bands towards lower wavenumbers is observed in the heterostructure, indicating interfacial strain and charge transfer effects between ZnS and the MWCNTs. The Raman spectrum of the pure MWCNTs is provided in Fig. S1 for comparison.

Fig. 2(a) shows the SEM image of pristine ZnS which consists of spherical shape nanoparticles agglomerated together in a network like structure due to high surface energy. Fig. 2(b) displays the surface morphology of the ZnS/MWCNT heterostructure. It can be clearly observed that the incorporated MWCNTs reveal a three-dimensional interconnected network forming a porous matrix. Moreover, spherical ZnS NPs with average size about 5–10 nm are uniformly anchored onto the surface of the MWCNTs. This well-defined heterostructure facilitates enhanced electrical conductivity through the MWCNT network while providing abundant active sites for electrochemical reactions due to the ZnS nanoparticles. The porous and interconnected structure is expected to promote efficient ion diffusion and electron transport, making the material promising for energy storage applications such as lithium-ion batteries. Fig. 2(c) represents the corresponding EDX spectrum of the ZnS/MWCNTs heterostructure, which consists of C, Zn, and S peaks. The existence of the respective elements confirms the successful formation of a ZnS/MWCNT heterostructure. Moreover, Fig. S2 shows the EDX spectrum of ZnS. Fig. 2(d) demonstrates the corresponding TEM image of ZnS NPs with a diameter in the range of 5–50 nm. Fig. 2(e) illustrates the high-resolution TEM image of ZnS. The calculated lattice fringes with a d-spacing of 0.284 nm correspond to the (111) plane of cubic ZnS. Fig. 2(f) exhibits the HRTEM image of pristine MWCNTs with a diameter in the range of 10–15 nm. The multiple fringes confirm the multilayer of MWCNTs. Fig. 2(g) exhibits the TEM image of the ZnS/MWCNT heterostructure. It can be revealed that the heterostructure is composed of evenly distributed ZnS nanospheres on the MWCNTs and agrees well with the SEM observations. Fig. 2(h) shows the HRTEM image of the heterostructure and clearly shows the interface between ZnS and the MWCNTs. Fig. 2(i) displays the magnified HRTEM image of the ZnS/MWCNTs obtained from the area indicated in Fig. 2(h). The interplanar distance (d) was calculated to be 0.291 nm, which agrees well with the (111) plane of ZnS, while multilayer fringes confirm the formation of a heterostructure.

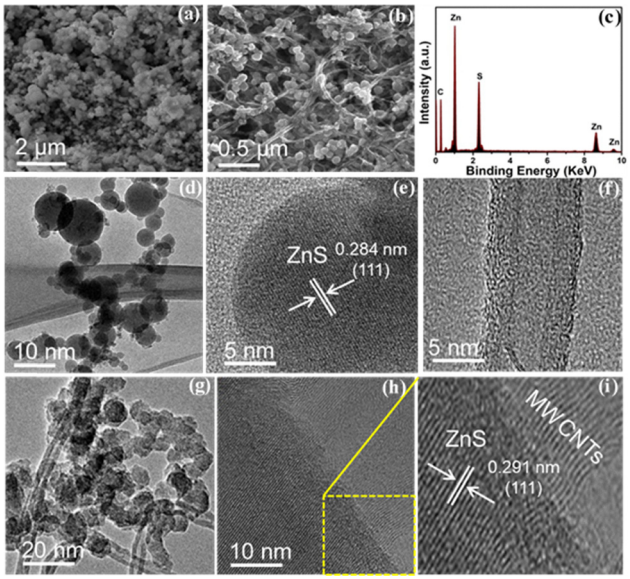

Fig. 2 SEM images of (a) ZnS and (b) heterostructured ZnS/MWCNTs (c) EDX spectrum of the ZnS/MWCNTs, (d) TEM image of ZnS, (e) and (f) HRTEM image of ZnS and MWCNT, (g) TEM image of ZnS/MWCNTs and (h), (i) HRTEM images of ZnS/MWCNTs.

To evaluate the specific surface area and particle size distribution of the samples, nitrogen adsorption–desorption isotherms were measured as illustrated in Fig. S3. The presence of distinct hysteresis loops in the relative pressure range of approximately 0.9–1.0 P/P_0 suggests capillary condensation within the mesopores. Both adsorption and desorption curves display type IV isotherms with hysteresis loops, characteristic of mesoporous materials. This indicates that the materials possess well-developed mesoporosity, which is advantageous for

facilitating Li-ion transport and enhancing electrolyte diffusion. The measured specific surface area of the heterostructure (78 $m^2 g^{-1}$) is larger than that of pristine ZnS (47 $m^2 g^{-1}$). The improved surface area is attributed to the incorporation of MWCNTs in the ZnS heterostructure. According to the BJH method, the average pore size is primarily distributed between 7–20 nm, confirming the mesoporous nature. This porous architecture not only offers abundant active sites for ZnS nanoparticle attachment but also provides internal space to accommodate volume changes during Li-ion insertion and extraction cycles.

3.2. Electronic structure and chemical composition analysis

The chemical composition and functional groups in the as-prepared ZnS and ZnS/MWCNT heterostructures were examine by FTIR. Fig. S4 shows the FTIR spectra of the ZnS and ZnS/MWCNTs. These spectra show the IR absorption due to the various vibration modes. The bands at 2360, 2069, and 1101 cm^{-1} can be assigned to the O═C═O stretching band, C–H bending[51] and C–O stretching vibrations, respectively. The bands at 989 cm^{-1} are attributed to C–H in-plane bending vibration of an aromatic ring. The characteristic major peak at 464 cm^{-1} corresponds to the Zn–S molecular stretching vibrations. The presence of –OH stretching vibrations at around 3400 cm^{-1} is related to associated water.[52] In the case of the ZnS/MWCNT spectrum, all the bands at the respective positions confirm the presence of ZnS.[53] However, owing to the presence of MWCNTs, the ZnS band might shift slightly due to interactions between ZnS and the MWCNTs. Also in comparison to ZnS, there is a broad absorption peak at 3100 cm^{-1} that corresponds to the stretching modes of hydroxyl groups (–OH) or the trapped water arising from the absorption of water on the surface of the MWCNTs.

The electrochemical performance of the material is strongly affected by the surface properties of the nanostructures. Thus, XPS analysis of the ZnS/MWCNTs was conducted to investigate the surface elemental composition and their electronic states. Fig. 3(a) displays the survey spectra of the ZnS/MWCNT heterostructure. The presence of Zn, S, and C peaks confirms the formation of the heterostructure. The de-convoluted XPS spectrum of Zn 2p is shown in Fig. 3(b). The spectrum displays two distinct peaks at 1023 and 1046 eV, associated with the electronic states of Zn $2p_{3/2}$ and Zn $2p_{1/2}$, respectively. The high resolution XPS spectrum of S 2p is presented in Fig. 3(c). As observed, the spectrum exhibits two distinct binding energy peaks at 162.7 and 163.65 eV representing S $2p_{3/2}$ and S $2p_{1/2}$ states, respectively.[1] The binding energy difference between the two peaks is in good agreement with the literature.[23] The high resolution C 1s spectra exhibit peaks at binding energies of 284.7, 288.9 and 285.4 eV corresponding to C–C, C═C and C–O, respectively,[34] as shown in Fig. 3(d).

3.3. Electrochemical performance of the cells

3.3.1 Cyclic voltammetry. The electrochemical behavior of the fabricated ZnS/MWCNTs and ZnS coin cells was recorded by conducting CV curves. Fig. 4(a) displays the CV curves of the

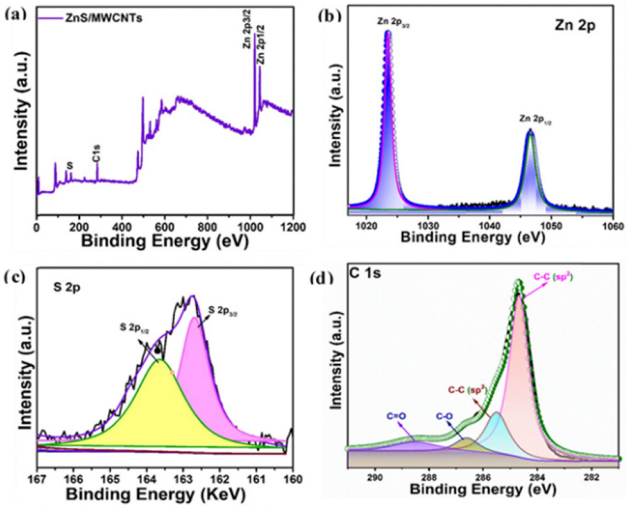

Fig. 3 (a) Survey spectrum of the ZnS/MWCNT heterostructure and high-resolution XPS-spectra of (b) Zn 2p, (c) S 2p and (d) C 1s.

ZnS/MWCNTs cell for the first three discharge/charge cycles at a scan rate of 0.5 mV s^{-1} between 0.01 to 3.0 V. During the first cathodic process, the CV curves exhibit two distinct cathodic peaks at 1.32 and 2.06 V. The first reduction peak at 2.06 V can be attributed to the redox reaction or reduction of ZnS into Zn and the formation of Li_2S, while the second reduction peak at 1.32 V corresponds to the decomposition of the electrolyte and formation of the solid electrolyte interface (SEI) on the surface of the electrode and alloying through the reaction of Zn with Li, resulting in the formation of a Li–Zn alloy.[1] During the oxidation reaction, anodic peaks located at 1.5, 1.97, and 2.46 V are identified, which are linked to the multi-step de-alloying process of the Li–Zn alloy (LiZn, Li_2Zn_3, $LiZn_2$, and Li_2Zn_5). Furthermore, a strong anodic peak centered at ~1.467 V can be ascribed to the conversion reaction between Zn and Li_2S forming ZnS. After completing the first cycle, the CV curves exhibited substantial overlap with an unchanged CV shape, indicating excellent electrochemical reversibility and stability of the ZnS/MWCNT cell throughout the lithiation/delithiation mechanism.[23] In contrast, Fig. 4(b) displays the CV curves of ZnS for the first five cycles at a scan rate of 0.5 mV s^{-1} between 0.01 to 3 V. The CV curves display comparable electrochemical behavior. In the charging process, Li^+ ions are released back to the anode, and a conversion reaction takes place. ZnS is transformed into metallic Zn, and lithium sulfide (Li_2S) is formed. During discharging or delithiation, Li ions move from the anode to the cathode, Zn is oxidized, and Li-ions are released back into the electrolyte. MWCNTs are used as conductive additives due to excellent conductivity and high surface area. The overall reaction can be described as:[23]

$$(x + 2)Li^+ + ZnS + (x + 2)e^- \leftrightarrow Li_2S + Li_xZn \quad (1)$$

$$ZnS + 2Li^+ + 2e^- \rightarrow Zn + Li_2S \quad (2)$$

$$Zn + Li_2S \rightarrow ZnS + 2Li^+ + 2e^- \quad (3)$$

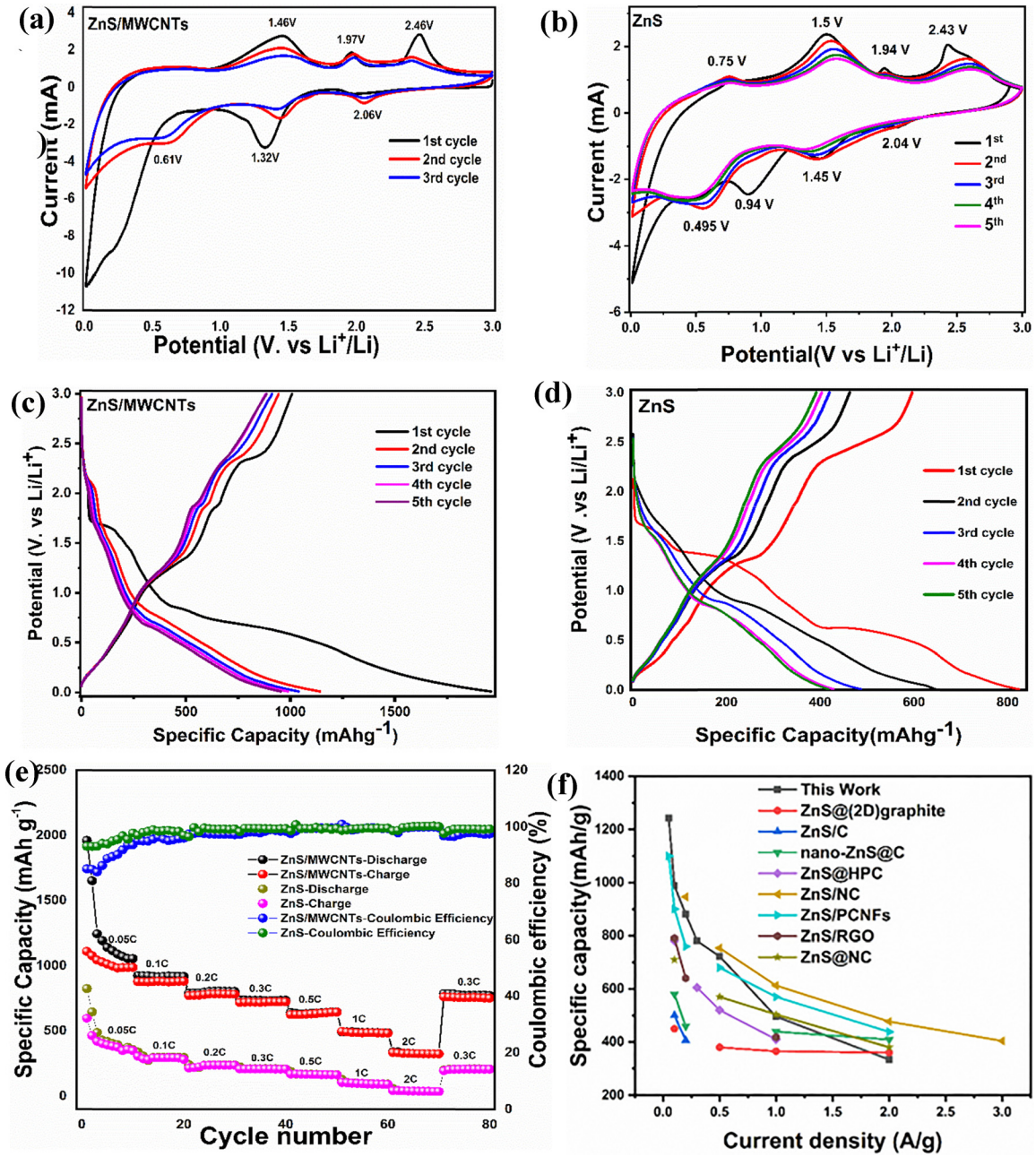

Fig. 4 CV response of (a) ZnS/MWCNTs and (b) ZnS cells, GCD profiles of (c) ZnS/MWCNTs and (d) pristine ZnS cells. (e) Rate Capability of ZnS and ZnS/MWCNTs. (f) The rate performance comparison of the ZnS/MWCNTs composite with previously reported ZnS-based composites.

3.3.2 Galvanostatic charge/discharge. The galvanostatic charge/discharge (GCD) profiles of the ZnS/MWCNTs and pristine ZnS cells were recorded in the voltage window of 0.01–3.0 V at a current density of 0.05C (50 mA g^{-1}). Fig. 4(c) presents the GCD curves of the ZnS/MWCNT cell for the initial five cycles within the voltage range of 0.01–3.0 V *vs.* Li/Li^+. The appearance of multiple distinct redox plateaus indicates the occurrence of progressive structural transformation reactions, consistent with the mechanisms outlined in eqn (1)–(3). The well-preserved shape of these plateaus across cycles reflects the good structural stability of the ZnS/MWCNT anode. Furthermore, the redox plateaus observed in the GCD profiles correspond well with the peaks identified in the cyclic voltammetry (CV) curves. As observed, the initial discharge capacity of the ZnS/MWCNTs anode reaches approximately 1960 mA h g^{-1} at 0.05 A g^{-1}. The capacity remains stable over subsequent cycles, confirming the excellent electrochemical stability of the ZnS/MWCNT anode. For comparison, the GCD profiles of the pristine ZnS cell were also recorded as shown in Fig. 4(d). The first specific discharge capacity of the pristine cell is about 823 mA h g^{-1}. Notably, the initial capacity of the ZnS/MWCNT electrode is significantly higher

Table 1 Comparative analysis of the electrochemical performance of the ZnS-based heterostructure used in LIBs

Electrode materials	Current density (A g^{-1})	Reversible capacitance (mA h g^{-1})	Cycling performance (mA h g^{-1})	No. of cycles	Ref.
ZnS@HPC	1.5	370	408@1 A g^{-1}	200	55
ZnS/graphene	1	418	570@0.2 A g^{-1}	200	56
ZnS-C nanoparticles	5	363	506@0.5 A g^{-1}	600	57
ZnS@NC	2	380	520@1 A g^{-1}	200	58
ZnS QDs/graphene	1	376	759@0.1 A g^{-1}	100	59
ZnS/PCNFs	2	438	718@0.2 A g^{-1}	150	60
ZnS-defective CNTs	8	377.8	451.3@5 A g^{-1}	1200	18
ZnS/N doped C	3	404	377.1@1.0 A g^{-1}	400	1
CNT/ZnS-QDs	0.5	771	—	150	39
ZnS nanosphere/MWCNTs	4	320	397@0.1 A g^{-1}	300	37
Core shell MWCNTs-ZnS	0.1	520	414@0.1	200	38
ZnS@graphite	3	330	444@0.1 A g^{-1}	300	61
ZnS/C	8	235.2	304.4@0.4 A g^{-1}	300	25
ZnS/MWCNTs	0.1	1060	610@0.3 A g^{-1}	1000	This work

than that of pristine ZnS and the previously reported works as shown in Table 1.

3.3.3 Rate performance. Fig. 4(e) illustrates the comparative rate performance of the ZnS/MWCNT and ZnS anodes at various current densities ranging from 0.05 to 2 A g^{-1} up to 80 cycles. The results clearly indicate that the reversible capacities gradually decrease with the increase in current rate. The ZnS/MWCNTs anode shows reversible capacities of 1060, 866, 747, 680, 576, 393, and 287 mA h g^{-1} at current rates from 0.05 to 2.0 A g^{-1}, respectively. In comparison, the reversible capacity of the ZnS anode decreases sharply from 478, 390, 307, 255, 206, 179 and 140 mA h g^{-1} at 0.05 to 2 A g^{-1}, respectively. It can be revealed that the ZnS/MWCNT anode demonstrates improved rate capability as compared to the pristine ZnS anode. Fig. 4(f) illustrates the rate performance comparison plot of specific capacity of various ZnS-based anode materials as a function of current density. It is evident that the developed ZnS/MWCNT heterostructure exhibits superior electrochemical performance compared to previously reported materials. Across all tested current densities, the ZnS/MWCNTs electrode consistently delivers higher specific capacities, highlighting its excellent rate capability. For instance, at lower current densities, the specific capacity of the ZnS/MWCNT electrode exceeds 1060 mA h g^{-1}, which gradually decreases with increasing current density but still remains significantly higher than other ZnS-based materials, such as ZnS@2D graphite, ZnS/C, nano-ZnS@C, ZnS@HPC, ZnS/NC, ZnS/PCNFs, ZnS/RGO, and ZnS@NC. These results confirm the remarkable lithium storage performance and enhanced structural stability of the ZnS/MWCNTs heterostructure, making it a promising candidate for high-performance lithium-ion battery anodes.

3.3.4 Cycling stability. To examine the prolong cycling stability of the ZnS/MWCNTs anode, the GCD profile was tested at 0.3 A g^{-1} up to 1000 cycles as shown in Fig. 5(a). As observed, the ZnS/MWCNTs anode shows an initial specific capacity of approximately 680 mA h g^{-1}, which gradually decreases during cycling. After 1000 cycles, the specific capacity stabilizes at around 610 mA h g^{-1}, indicating good capacity retention of about 94% and a coulombic efficiency of ~98%. The relatively slow decline in capacity demonstrates the electrode's potential for use in rechargeable lithium-ion batteries with stable performance over extended cycles. Moreover, the morphological features of the ZnS/MWCNT electrode are also evaluated by recording the SEM image after 1000 cycles. Fig. S5 shows the SEM image and reveals that despite repeated lithiation/delithiation, the morphology of the ZnS/MWCNT structure remained unchanged. The reliable behavior of the assembled electrode reveals the structural stability of the ZnS/MWCNT structure and is considered a potential candidate for high-performance LIBs.

3.3.5 Electrochemical impedance analysis. To explore the kinetics of the fabricated ZnS and ZnS/MWCNTs electrodes, electrochemical impedance spectra (EIS) were measured within a frequency range of 0.08 Hz to 3.1 kHz. The Nyquist plots presented in Fig. 5(b) reveal that the ZnS/MWCNT electrode has a small semicircle radius relative to the pristine ZnS electrode. Moreover, both the impedance plots exhibit a depressed semicircular arc. Therefore, instead of capacitance in the equivalent circuits, constant phase element (CPE) is used to describe the non-ideal capacitive behavior, which is given by: $C = R^{(1-n)/n}(\mathrm{CPE})^{1/n}$, where R and C are the equivalent capacitance and resistance of the associated component and "n" is a dimensionless exponent that quantifies the deviation from ideal Debye behavior with value 0–1. The fitted circuit suggests that the experimental data correspond to a configuration consisting of one parallel RC circuit in combination with a series-connected resistance (R_s) which is actually the bulk resistance of the cell, accounting for contributions from the electrolyte, separator and electrodes and is indicated by the high-frequency intercept on the real axis. At medium frequency, the semicircle is associated with charge transfer resistance (R_{ct}) and double-layer capacitance. The low-frequency region is characterized by a slope line inclined at approximately 45° representing Warburg impedance (Z_W), which corresponds to the diffusion mechanism of Li^+. Table 2 displays the extracted EIS fitting values for both electrodes. A reduction in Rct with increasing carbon content suggests an enhanced charge transfer rate and improved electrical conductivity of the synthesized electrodes. Hence the formation of the ZnS/MWCNT electrode significantly enhances the electrochemical behavior and the charge–discharge dynamics of LIBs. The strong interfacial coupling

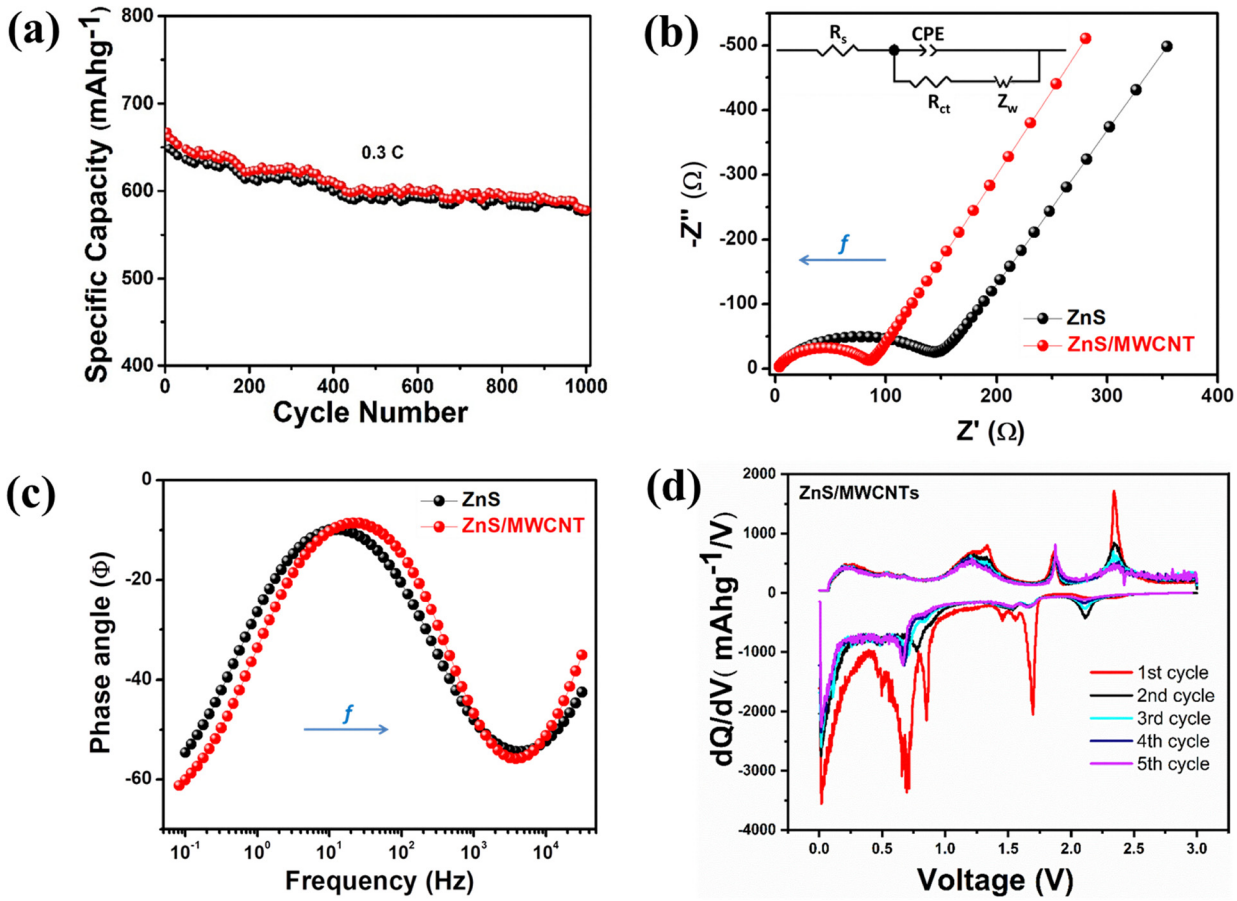

Fig. 5 (a) Long-term cycling stability of ZnS/MWCNTs for 500 cycles at 0.3C. (b) Electrochemical impedance spectra (Nyquist plot) of the pristine ZnS and ZnS/MWCNT heterostructure. (c) Bode angle plot vs frequency of the pristine ZnS and ZnS/MWCNT heterostructure electrodes. (d) (dQ/dV) plot of the ZnS/MWCNT heterostructure electrode.

Table 2 EIS fitting parameters of the ZnS and ZnS/MWCNT electrodes

Cathode	R_{ct} (Ω)	R_s (Ω)
ZnS	146	2.45
ZnS/MWCNTs	83.2	2.75

facilitates efficient charge transfer by reducing interfacial resistance, while the intimate contact between the ZnS nanoparticles and the conductive MWCNT network provides continuous electron pathways and mechanical buffering against volume changes.

The Bode phase angle plot offers a quick and comprehensive way to understand the electrochemical behavior of the system at specific frequencies as shown in Fig. 5(c). Notably, a 0° phase angle signifies an ideal resistor, +90° an ideal inductor and −90° an ideal capacitor. In our case, despite instrumental limitations at very high frequencies, we expect that the phase angle approaches to 0° showing the resistive behavior as represented by R_s in the equivalent circuit model. In the intermediate frequency range, a prominent phase shift is observed indicating mixed behavior or non-ideality within the system as fitted by CPE in the equivalent circuit model. In the low frequency range, the behavior is characteristic of diffusion-controlled processes and indicative of Warburg impedance. Such a response reflects mass transport limitations, such as the diffusion of ions through the electrolyte or within a porous electrode structure. Thus, it is clearly seen that the ZnS/MWCNTs heterostructure electrode shows better characteristics than the ZnS heterostructure electrode.

3.3.6 Differential capacity curve. Fig. 5(c) illustrates the differential capacity (dQ/dV) *versus* voltage curve of the ZnS/MWCNT heterostructure. The plot provides more insight into the electrochemical processes occurring during lithium-ion battery cycling. In the first cycle, the curve exhibits prominent and sharp peaks, particularly in the low voltage range between 0.3 V and 1.0 V, which are attributed to the conversion reaction of ZnS into Zn and Li_2S, along with the formation of the solid electrolyte interphase (SEI) layer. These processes are mostly irreversible, leading to a significant capacity loss during the initial cycle, which is very common in conversion-type anode materials. At higher voltages around 2.0 V to 2.5 V, some additional peaks are observed, corresponding to the oxidation of Zn and Li_2S during the delithiation process. In subsequent cycles (2nd to 5th), the dQ/dV curves become more stable and reproducible, with well-defined peaks at similar voltage positions. This stable behavior indicates the reversible lithium

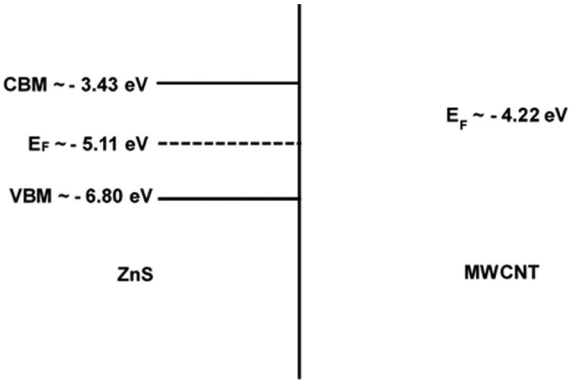

Fig. 6 Energy level alignment at the ZnS/MWCNT interface calculated with the hybrid HSE06 functional. The dashed horizontal line represents the Fermi level (EF) of each material.

insertion/extraction processes and structural stability of the electrode material. The overlapping nature of the dQ/dV curves from the second cycle onward highlights the enhanced cycling stability and electrochemical reversibility of the ZnS/MWCNT heterostructure. The results confirm that the incorporation of MWCNTs enhances structural integrity and electrochemical reversibility, making the material suitable for long-term lithium-ion battery applications.

3.3.7 Density functional theory analysis. In order to further elucidate the experimental findings, density functional theory (DFT) calculations were carried out. Fig. 6 depicts energy level alignment of the ZnS/MWCNT interface. We noted that functionalization of the MWCNTs may open up a small band gap, but this should not significantly alter the energy level alignment. As evident, the Fermi level (EF) of the MWCNTs is noticeably higher than that of ZnS. These results suggest that an electron transfer will take place from the MWCNTs to ZnS as an interface is formed. Therefore, the electron density of ZnS will increase owing to the interfacial charge transfer. Considering the higher electrical conductivity arising from the inclusion of conductive MWCNTs as well as enhanced electron density on ZnS, as a result of charge transfer across the interface, the kinetics of the redox reactions of the ZnS/MWCNT-based electrode will improve in comparison to the pristine ZnS electrode.[54] This is evident from the results of the impedance analysis (Fig. 5(b)) where a noticeable drop in charge transfer resistance is perceived for the ZnS/MWCNTs electrode in comparison to that of the pristine ZnS. Besides improved redox reaction kinetics, addition of MWCNTs will also introduce new active sites not only within MWCNTs but also around the edges of the absorbed ZnS nanoparticles. This will improve the specific capacity of the electrode, which is confirmed by the experimental results. A schematic depiction of the heterostructure between the MWCNTs and ZnS(110) surface is also presented in Fig. S6.

4. Conclusion

This study presents the development of a synergistic ZnS/MWCNT heterostructure as a high-performance anode material for lithium-ion batteries (LIBs). By integrating the high theoretical capacity of ZnS with the excellent electrical conductivity, mechanical robustness, and structural stability of MWCNTs, the composite effectively overcomes the intrinsic limitations of ZnS, such as poor conductivity and severe volume expansion. Electrochemical evaluations reveal outstanding cycling stability, a high initial discharge capacity, and superior rate performance. Additionally, density functional theory (DFT) calculations confirm the presence of favorable lithium adsorption sites and low diffusion energy barriers, which contribute to the enhanced performance. Notably, the fabrication process is scalable and utilizes cost-effective, readily available materials, underscoring the practical feasibility of this heterostructure for commercial application. These findings highlight the potential of the ZnS/MWCNT heterostructure as a promising anode material for long-life, high-performance LIBs.

Author contributions

Marrium Shabbir led the methodology and investigation, and prepared the original draft. Rizwan Akram contributed to data curation and formal analysis. Saqib Javed was responsible for software implementation and performed the DFT calculations. Zahid Abbas assisted in the fabrication of coin cells. Amina Zafar carried out impedance analysis. Sheeraz Mehboob provided formal analysis. Shafqat Karim supported manuscript review and editing. Luqman Ali and Shahid Ali assisted in experimental work and data management. Imran Shakir contributed in formal data analysis. Amjad Nisar and Mashkoor Ahmad jointly supervised the overall project, provided conceptual guidance, contributed to writing and editing, and managed project administration and funding acquisition.

Conflicts of interest

No financial conflicts of interest are declared by the authors.

Data availability

The authors confirm that the data supporting the findings of this study are available within the article and its supplementary information (SI). Supplementary information contains Raman spectrum of pure MWCNTs, Edx spectra of pristine ZnS, BET specific surface area of ZnS and ZnS/MWCNTs, inset is pore size distribution, FTIR spectrum of pristine ZnS and ZnS/MWCNTs heterostructure, SEM of the ZnS/MWCNTs structure and a schematic depiction of heterostucture between MWCNTs/ZnS(110) surface. See DOI: **https://doi.org/10.1039/d5ma00889a**.

Acknowledgements

This work was supported by the Pakistan Atomic Energy Commission (PAEC). The authors gratefully acknowledge COMSTECH, Pakistan, and SESAME, Jordan, for facilitating

the experiments at the MS beamline under the SESAME Users' Program.

References

1 L. Wang, D. Li, Q. Li, Q. Pan, M. Zhang and L. Zhang, *et al.*, *J. Alloys Compd.*, 2022, **910**, 164783.
2 P. Li, H. Kim, S.-T. Myung and Y.-K. Sun, *Energy Storage Mater.*, 2021, **35**, 550–576.
3 X.-B. Cheng, R. Zhang, C.-Z. Zhao and Q. Zhang, *Chem. Rev.*, 2017, **117**, 10403–10473.
4 J. Lu, Z. Chen, F. Pan, Y. Cui and K. Amine, *Electrochem. Energy Rev.*, 2018, **1**, 35–53.
5 C. Ke, R. Shao, Y. Zhang, Z. Sun, S. Qi, H. Zhang and M. Li, *et al.*, *Adv. Funct. Mater.*, 2022, **32**, 2205635.
6 C. Zu, H. Yu and H. Li, *InfoMat*, 2021, **3**, 648–661.
7 L. Zhang, M. Zhang, F. Peng, Q. Pan, H. Wang, F. Zheng, Y. Huang and Q. Li, *J. Alloys Compd.*, 2022, **910**, 164908.
8 D. Wang, M. Gao, H. Pan, J. Wang and Y. Liu, *J. Power Sources*, 2014, **256**, 190–199.
9 C. Wang, Y. Zhang, Y. Li, Y. Zhang, Y. Dong, D. Li and J. Zhang, *J. Alloys Compd.*, 2020, **820**, 153147.
10 J. Ma, J. Sung, J. Hong, S. Chae, N. Kim, S.-H. Choi and G. Nam, *et al.*, *Nat. Commun.*, 2019, **10**, 475.
11 Y. Ding, Z. P. Cano, A. Yu, J. Lu and Z. Chen, *Electrochem. Energy Rev.*, 2019, **2**, 1–28.
12 S. Gu and A. Zhu, *J. Alloys Compd.*, 2020, **813**, 152160.
13 P. Ren, Z. Wang, B. Liu, Y. Lu, Z. Jin, L. Zhang, L. Li, X. Li and C. Wang, *J. Alloys Compd.*, 2020, **812**, 152014.
14 X. Zou, Y. Huang, Y. Chen, C. Cai, M. Qiu, Y. Zhang and J. Zhu, *Appl. Surf. Sci.*, 2023, **614**, 156169.
15 J. Tan, X. He and M. Zhao, *Diamond Relat. Mater.*, 2012, **29**, 42–47.
16 J. He and Z. Jiao, *Appl. Surf. Sci.*, 2022, **580**, 152371.
17 S. Feng, Z. Wang, H. Guo, X. Li, G. Yan and J. Wang, *Energy Fuels*, 2021, **36**, 677–683.
18 W. Zhang, Z. Huang, H. Zhou, S. Li, C. Wang, H. Li, Z. Yan, F. Wang and Y. Kuang, *J. Alloys Compd.*, 2020, **816**, 152633.
19 J. Li, D. Yan, S. Hou, T. Lu, Y. Yao, D. H. C. Chua and L. Pan, *Chem. Eng. J.*, 2018, **335**, 579–589.
20 T. T. Q. Hoa, T. D. Canh and N. N. Long, *J. Phys.: Conf. Ser.*, 2009, **187**, 012081.
21 S. Biswas and S. Kar, *Nanotechnology*, 2008, **19**, 045710.
22 W. B. Tan, N. Huang and Y. Zhang, *J. Colloid Interface Sci.*, 2007, **310**, 464–470.
23 W. Zhang, J. Zhang, Y. Zhao, T. Tan and T. Yang, *Materials*, 2018, **11**, 1537.
24 H. Li, Z. Liu, S. Yang, Y. Zhao, Y. Feng, Z. Bakenov, C. Zhang and F. Yin, *Materials*, 2017, **10**, 1102.
25 L. He, X.-Z. Liao, K. Yang, Y.-S. He, W. Wen and Z.-F. Ma, *Electrochim. Acta*, 2011, **56**, 1213–1218.
26 A.-R. Park, K.-J. Jeon and C.-M. Park, *Electrochim. Acta*, 2018, **265**, 107–114.
27 L. Chen, H. Zhou, C. Fu, Z. Chen, C. Xu and Y. Kuang, *Int. J. Hydrogen Energy*, 2016, **41**, 21850–21860.
28 Z. Ren, Z. Wang, C. Chen, J. Wang, X. Fu, C. Fan and G. Qian, *Electrochim. Acta*, 2014, **146**, 52–59.
29 X. Du, H. Zhao, Y. Lu, Z. Zhang, A. Kulka and K. Świerczek, *Electrochim. Acta*, 2017, **228**, 100–106.
30 P. Naveenkumar, M. Maniyazagan, N. Kang, H.-W. Yang, W.-S. Kang and S.-J. Kim, *Int. J. Mol. Sci.*, 2022, **23**, 13945.
31 I. Anshori, L. N. Rizalputri, R. R. Althof, S. S. Surjadi, S. Harimurti, G. Gumilar, B. Yuliarto and M. Handayani, *Nanocomposites*, 2021, **7**, 97–108.
32 A. Sapalidis, Z. Sideratou, K. N. Panagiotaki, E. Sakellis, E. P. Kouvelos, S. Papageorgiou and F. Katsaros, *Front. Mater.*, 2018, **5**, 11.
33 S. A. Chernyak, A. S. Ivanov, K. I. Maslakov, A. V. Egorov, Z. Shen, S. S. Savilov and V. V. Lunin, *Phys. Chem. Chem. Phys.*, 2017, **19**, 2276–2285.
34 T. Hou, B. Liu, X. Sun, A. Fan, Z. Xu, S. Cai, C. Zheng, G. Yu and A. Tricoli, *ACS Nano*, 2021, **15**, 6735–6746.
35 A. Sadaqat, G. Ali, Z. Ali, F. J. Iftikhar and M. ul Hasan, *ACS Appl. Energy Mater.*, 2021, **4**, 13868–13877.
36 F. Ali, A. Zafar, A. Nisar, Y. Liu, S. Karim, F. Faiz and Z. Zafar, *et al.*, *New J. Chem.*, 2023, **47**, 681–690.
37 A. Fan, T. Hou, X. Sun, D. Xie, X. Li, N. Zhang and J. Guo, *et al.*, *ChemElectroChem*, 2020, **7**, 1904–1913.
38 Y. Cao, S. Wang, C. Liu and A. Li, *J. Mater. Res.*, 2021, **36**, 1262–1271.
39 T. Shi, C. Zhao, C. Yin, H. Yin, C. Song, L. Qin, Z. Wang, H. Shao and K. Yu, *Nanotechnology*, 2020, **31**, 495406.
40 C. Qin, D. Wang, Z. Xu and G. Tang, *Appl. Sci.*, 2020, **10**, 682.
41 G. Kresse and J. Furthmüller, *Comput. Mater. Sci.*, 1996, **6**, 15–50.
42 J. P. Perdew, K. Burke and M. Ernzerhof, *Phys. Rev. Lett.*, 1996, **77**, 3865.
43 A. V. Krukau, O. A. Vydrov, A. F. Izmaylov and G. E. Scuseria, *J. Chem. Phys.*, 2006, **125**, 224106.
44 L. Chen, C. Xu, L. Yang, M. Zhou, B. He, Z. Chen, Z. Li, M. Shi, Z. Hou and Y. Kuang, *Appl. Surf. Sci.*, 2018, **454**, 284–292.
45 N. L. W. Septiani, Y. V. Kaneti, B. Yuliarto, H. K. Dipojono, T. Takei, J. You and Y. Yamauchi, *Sens. Actuators, B*, 2018, **261**, 241–251.
46 A. Fairbrother, V. Izquierdo-Roca, X. Fontané, M. Ibáñez, A. Cabot, E. Saucedo and A. Pérez-Rodríguez, *CrystEngComm*, 2014, **16**, 4120–4125.
47 V. D. Chinh, G. Speranza, C. Migliaresi, N. V. Chuc, V. M. Tan and N.-T. Phuong, *Sci. Rep.*, 2019, **9**, 5667.
48 N. Naeem, S. Butt, Z. Afzal, M. W. Akram, M. Irfan, M. A. U. Rehman and M. U. Farooq, *RSC Adv.*, 2025, 569–578.
49 R. Fernández-Loyola, M. Muthuvel, A. B. Hernández-Maldonado, J. A. Menchaca-Rivera, J. F. Perez-Robles, O. Solorza-Feria and G. G. Botte, *Ceram. Int.*, 2021, 13604–13612.
50 H. Mustafa, Y. Yu, A. Zafar, Y. Liu, S. Karim, S. Javed and M. Ahmad, *New J. Chem.*, 2022, 3417–3425.
51 B. Kwamboka, W. Omwoyo and N. Oyaro, *Indian J. Nanosci.*, 2016, **4**, 2.

52 V. D. Mote, Y. Purushotham and B. N. Dole, *Cerâmica*, 2013, **59**, 395–400.
53 R. Sharma, *Int. Multidiscip. Res. J.*, 2011, **1**(9), 8–11.
54 R. He, B. Yu, Z. Li and Y. Zhao, *Energy Environ. Mater.*, 2019, **2**(4), 264–279.
55 H. Chen, B. Zhang, Y. Cao, X. Wang, Y. Yao, W. Yu, J. Zheng, J. Zhang and H. Tong, *Ceram. Int.*, 2018, **44**, 13706–13711.
56 M. Mao, L. Jiang, L. Wu, M. Zhang and T. Wang, *J. Mater. Chem. A*, 2015, **3**, 13384–13389.
57 X. Du, H. Zhao, Z. Zhang, Y. Lu, C. Gao, Z. Li, Y. Teng, L. Zhao and K. Świerczek, *Electrochim. Acta*, 2017, **225**, 129–136.
58 J. Li, Y. Fu, X. Shi, Z. Xu and Z. Zhang, *Chem. – Eur. J.*, 2017, **23**, 157–166.
59 R. Zhang, Y. Wang, M. Jia, J. Xu and E. Pan, *Appl. Surf. Sci.*, 2018, **437**, 375–383.
60 L. Wang, J. Ju, N. Deng, G. Wang, B. Cheng and W. Kang, *Electrochem. Commun.*, 2018, **96**, 1–5.
61 J. Yoon, I. T. Kim, J. Bae and J. Hur, *J. Ind. Eng. Chem.*, 2019, **76**, 258–267.